

# Unlocking the Potential of Metal-Doping Fe<sub>2</sub>O<sub>3</sub>/Rice Husk Ash Catalysts for Low-Temperature CO-SCR Enhancement

Yuqing Pan, Na Li, Chenyang Wu, Qulan Zhou,\* and Ke Li\*

Cite This: *ACS Omega* 2024, 9, 16621–16630

Read Online

ACCESS |



Metrics &amp; More

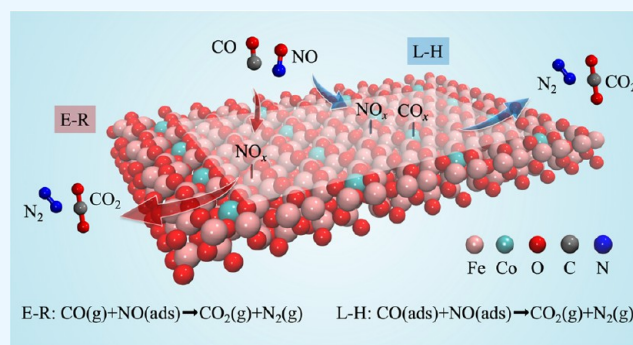


Article Recommendations



Supporting Information

**ABSTRACT:** Transition metal oxides are efficient bifunctional catalysts for the selective catalytic reduction (SCR) of nitrogen oxides (NO<sub>x</sub>) using CO. Nonetheless, their poor activity at lower temperatures constrains broader industrial application. Herein, we propose an optimized Fe<sub>2</sub>O<sub>3</sub>-based catalyst through strategic metal doping with Cu, Co, or Ce, which engenders a harmonious balance for the synergistic removal of CO and NO<sub>x</sub>. Among the developed catalysts, Co-doped Fe<sub>2</sub>O<sub>3</sub>, supported by rice husk ash, demonstrates superior low-temperature CO-SCR activity, achieving CO and NO<sub>x</sub> conversion ratios and N<sub>2</sub> selectivity above 98.5% at 100–500 °C. The enhanced catalytic performance is attributed to the catalyst's improved redox properties and acidity, engendered by strong Fe–O<sub>x</sub>–Co interactions. Furthermore, the CO-SCR reaction adheres to the Langmuir–Hinshelwood and Eley–Rideal mechanisms. Our findings shed light on the future industrial application of low-temperature CO and NO<sub>x</sub> near-zero emission technology and provide a strategy for the design of low-cost SCR catalysts.



## 1. INTRODUCTION

Nitrogen oxides (NO<sub>x</sub>) emitted from stationary sources (such as coal-fired power plants) and mobile sources (like automobile exhaust) are primary air pollutants that cause acid rain and photochemical smog, posing threats to both the ecological environment and human health.<sup>1–3</sup> Currently, selective catalytic reduction (SCR), due to its high purification efficiency and cost-effectiveness, is a widely adopted approach to eliminate NO<sub>x</sub> (NO and NO<sub>2</sub>).<sup>4–6</sup> The traditional SCR process uses NH<sub>3</sub> as the reducing agent, but NH<sub>3</sub>-SCR technology also suffers from the disadvantages of ammonia leakage, equipment corrosion, and high operating costs.<sup>7,8</sup> These limitations underscore the necessity for the innovation of enhanced SCR reductants that align with the imperatives of ecological sustainability. In this context, CO-SCR technology has emerged as a viable alternative, attracting considerable scholarly interest.<sup>9,10</sup> Carbon monoxide (CO) frequently emerges as a noxious byproduct from the incomplete combustion of carbon-rich fuels, notably in automobile and industrial emissions, such as those from sintering and coking processes.<sup>2</sup> The adoption of CO-SCR is considered an attractive technology for NO<sub>x</sub> removal. It presents economic advantages by eliminating the reliance on ammonia and boosts energy efficiency by reducing NO<sub>x</sub> emissions through residual carbon in the flue gas. Despite ongoing advancements, the widespread implementation of CO-SCR technology is still hindered by the essential need to design an efficient

bifunctional catalyst, pivotal for achieving simultaneous removal of NO<sub>x</sub> and CO.<sup>11</sup>

In recent years, many scholars have focused their research on the development and application of CO-SCR catalysts.<sup>12–15</sup> Compared with noble metals, transition metals have been extensively studied for NO reduction by CO, attributed to their high catalytic activity and low economic cost. Among them, Fe<sub>2</sub>O<sub>3</sub>-based catalysts stand out for their outstanding CO-SCR performance, achieving over 80% CO and NO<sub>x</sub> conversion at moderate to high temperatures (300–500 °C).<sup>16,17</sup> Despite these advantages, few Fe<sub>2</sub>O<sub>3</sub>-based catalysts are well suited for low-temperature sintering flue gas (120–180 °C), low-temperature coking flue gas (220–250 °C), and automobile exhaust gases with large temperature fluctuations (150–500 °C). The catalyst's high-activity window at low temperatures (<300 °C) can allow the denitration equipment to be efficiently placed at downstream of the desulfurizer or ash separator to avoid the catalyst deactivation.<sup>18</sup> The development of Fe<sub>2</sub>O<sub>3</sub>-based catalysts has been hindered by their poor performance (<60% NO<sub>x</sub> conversion) at lower temperatures

Received: January 18, 2024

Accepted: January 30, 2024

Published: March 25, 2024



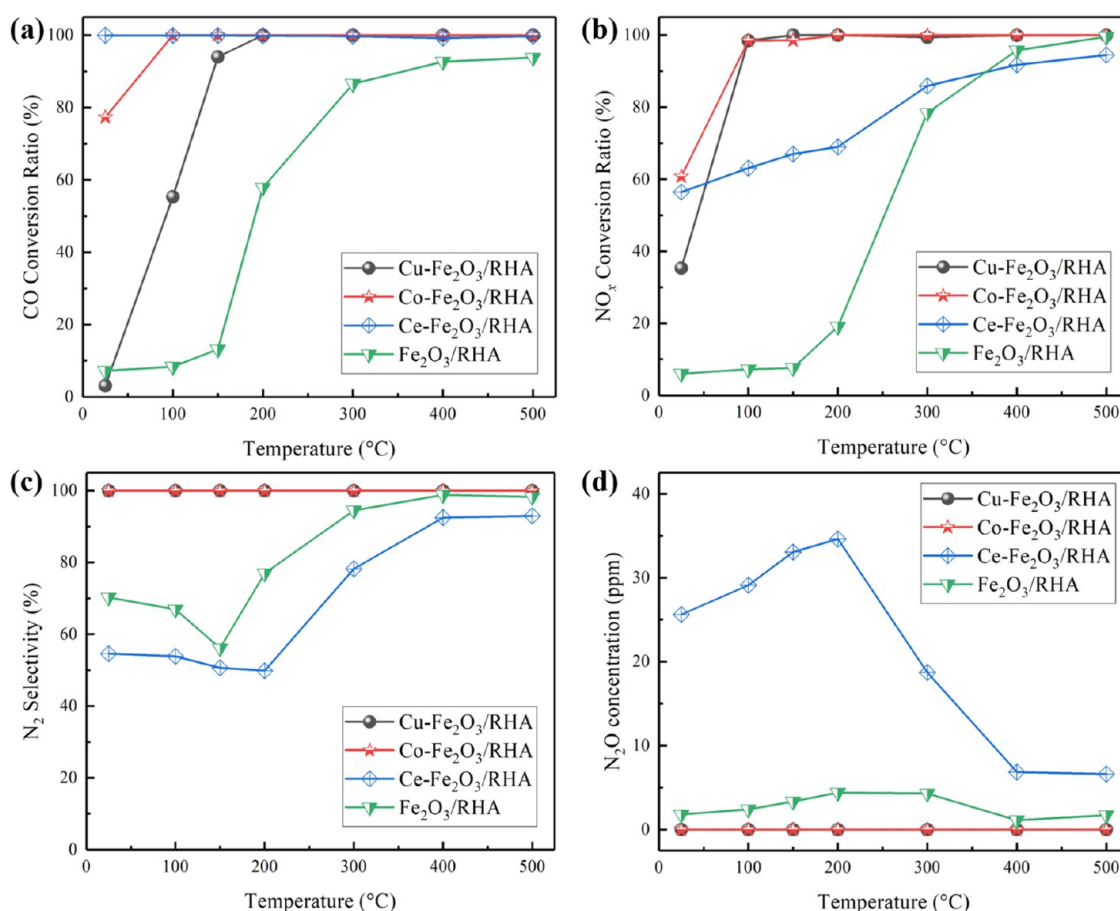


**Figure 1.** CO-SCR activity results of metal-doped Fe<sub>2</sub>O<sub>3</sub>-based catalysts: (a) CO conversion ratio, (b) NO<sub>x</sub> conversion ratio, (c) N<sub>2</sub> selectivity, and (d) N<sub>2</sub>O concentration.

(<300 °C) and weak resistance to deactivation by O<sub>2</sub>, SO<sub>2</sub>, and H<sub>2</sub>O.<sup>19</sup> These limitations in the Fe<sub>2</sub>O<sub>3</sub>-based catalysts urgently need to be solved, promoting further industrial application on a large scale.<sup>20</sup>

Metal doping has emerged as a potent strategy to enhance the low-temperature efficiency of Fe<sub>2</sub>O<sub>3</sub> catalysts for CO-SCR.<sup>13,21</sup> In recent research, scholars have demonstrated the promising results of metal-doping catalysts, using metals like Cu, Ce, and Co as active agents for the doping.<sup>22–25</sup> For example, Li and his team<sup>26</sup> synthesized a series of three-dimensional ordered macroporous (3DOM) MFe<sub>2</sub>O<sub>4</sub> (M = Co, Ni, Cu) spinel catalysts for CO-SCR. Among these, the CuFe<sub>2</sub>O<sub>4</sub> catalyst exhibited the most remarkable activity, enhancing the low-temperature performance of the Fe<sub>2</sub>O<sub>3</sub>-based catalyst by a minimum of 20%. Furthermore, ceria has garnered attention in the realm of catalysis, owing to its remarkable oxygen storage capacity and rapid conversion between Ce<sup>4+</sup> and Ce<sup>3+</sup> states.<sup>27,28</sup> Optimized 3DOM Ce<sub>0.6</sub>Fe<sub>0.4</sub>O<sub>2</sub> catalysts exhibited nearly 90% NO<sub>x</sub> conversion at 200 °C and high catalytic activity over a wide temperature window of 200–700 °C.<sup>29</sup> In a study by Dai and colleagues,<sup>30</sup> they prepared a variety of transition metal-doped CeO<sub>2</sub> catalysts using vermiculite as the support for CO-SCR. Their findings indicated a performance sequence as follows: Zn < Cr < Fe < no dopant < Mn < Ni < Co < Cu. Besides, Dong's team innovatively developed magnetic bayberry-like  $\gamma$ -xCoFe<sub>2</sub>O<sub>3</sub> microsphere catalysts with diverse mole ratios, where the 5Co–Fe showcased peak activity, attributed to its expansive

surface area.<sup>31</sup> Although some progress has been made in metal doping modification strategies, it is still difficult to strike a good balance between high CO-SCR activity over a wide temperature window, high resistance to SO<sub>2</sub>/H<sub>2</sub>O poisoning, and low economic cost of the catalysts.<sup>32,33</sup> Therefore, there is an urgent need to design novel catalyst formulations, i.e., to improve the active components while optimizing the performance of supports to accelerate the process of industrial application.

In this study, we sought to enhance the low-temperature CO-SCR efficiency of Fe<sub>2</sub>O<sub>3</sub>-based catalysts by optimizing the support and introducing doped metal. Our prior studies showed that rice husk ash (RHA), as a kind of low-cost biomass, can be recycled and reused. RHA rich in amorphous SiO<sub>2</sub> has a high specific surface area and porous structure, making it a high-performance catalyst support with excellent thermal stability.<sup>34</sup> Therefore, we prepared Cu/Co/Ce-doped Fe<sub>2</sub>O<sub>3</sub> catalysts supported on RHA and assessed their catalytic behaviors to determine the most effective metal dopant. Characterization methods were used to study the physical and chemical properties of the doped metal catalysts. Our findings identified Co as the optimal doping metal, with the Co–Fe<sub>2</sub>O<sub>3</sub>/RHA catalyst achieving 98.5% CO and NO conversion as well as N<sub>2</sub> selectivity across a wide temperature range from 100 to 500 °C. Remarkably, the Co–Fe<sub>2</sub>O<sub>3</sub>/RHA catalyst maintained more than 98% CO conversion and about 80.1% NO<sub>x</sub> conversion after 30 h of anti-poisoning test. Moreover, the cobalt oxide modification of the Fe<sub>2</sub>O<sub>3</sub>-based catalyst attained

a trade-off between the surface acidity and redox ability, resulting in improved adsorption and activation capacity of the reactant gases. This study paves the way for the development of cost-efficient and highly active low-temperature CO-SCR catalysts and provides new application strategies for the recycling and reuse of biomass.

## 2. EXPERIMENT

Herein, we obtained RHA by incinerating rice husks in a fixed-bed reactor. The method of RHA preparation is detailed in our prior work, noting that the RHA comprised 85.2% amorphous SiO<sub>2</sub>, 8.55% activated carbon, and others.<sup>34</sup> The Cu–Fe<sub>2</sub>O<sub>3</sub>/RHA, Co–Fe<sub>2</sub>O<sub>3</sub>/RHA, Ce–Fe<sub>2</sub>O<sub>3</sub>/RHA, and Fe<sub>2</sub>O<sub>3</sub>/RHA catalysts, each with about 20 wt % metal oxide active components, were synthesized through the excessive impregnation method.

The synthesized catalysts were examined using a synchronous thermal analyzer (TGA-DSC, NETZSCH-STA449F5) to investigate the alterations in the catalysts during the calcination phase and determine an optimal calcination temperature, ensuring the full conversion of nitrate to oxides. Catalyst samples, prior to calcination, were subjected to temperatures ranging from 30 up to 600 °C (heating rate 5 K·min<sup>-1</sup>) within an Al<sub>2</sub>O<sub>3</sub> crucible under an ambient mix of 80% dry N<sub>2</sub> and 20% O<sub>2</sub>. Data from the thermogravimetry–differential thermal calorimetry (TG-DSC) assessments can be found in the Supporting Information (SI), as depicted in Figure S1.

The CO-SCR activity of the bimetal oxide catalysts was evaluated by using the CO-SCR catalytic activity test system shown in Figure S2. The reliability of the active system has been verified through multiple tests. We studied the physicochemical properties of the fresh unused catalysts (Cu–Fe<sub>2</sub>O<sub>3</sub>/RHA, Co–Fe<sub>2</sub>O<sub>3</sub>/RHA, and Ce–Fe<sub>2</sub>O<sub>3</sub>/RHA) and the used catalysts (labeled as Cu–Fe<sub>2</sub>O<sub>3</sub>/RHA-U, Co–Fe<sub>2</sub>O<sub>3</sub>/RHA-U, and Ce–Fe<sub>2</sub>O<sub>3</sub>/RHA-U), which have been subjected to activity assessments for over 16 h. The catalysts' characterization employed a suite of techniques, including scanning electron microscopy (SEM), energy-dispersive X-ray spectroscopy (EDS), Cs-corrected scanning transmission electron microscopy (TEM), X-ray diffraction (XRD), X-ray photoelectron spectroscopy (XPS), N<sub>2</sub> adsorption–desorption (Brunauer–Emmett–Teller (BET)), H<sub>2</sub> temperature-programmed reduction (H<sub>2</sub>-TPR), NH<sub>3</sub> temperature-programmed desorption (NH<sub>3</sub>-TPD), CO<sub>2</sub> temperature-programmed desorption (CO<sub>2</sub>-TPD), and in situ diffuse reflectance infrared Fourier transform spectroscopy (in situ DRIFTS). A comprehensive description of the experimental procedures can be found in the Supporting Information.

## 3. RESULTS AND DISCUSSION

**3.1. Activity Tests for Screening the Optimal Dopant Metal.** **3.1.1. Effect of Cu/Co/Ce Doping on the Catalytic Performance for CO-SCR.** The effect of metal doping on Fe<sub>2</sub>O<sub>3</sub>-based catalysts' performance was probed through activity experiments, aiming to pinpoint the most effective dopant metal. Activity comparisons among four catalysts in a gas stream (comprising 200 ppm NO, 2000 ppm CO, 6% of O<sub>2</sub>, with N<sub>2</sub> as the balance gas) revealed distinctive catalytic activity (shown in Figure 1). As can be seen in Figure 1(a), the Ce–Fe<sub>2</sub>O<sub>3</sub>/RHA catalyst maintained consistent CO conversion ratios approaching 100% over the entire temperature range (25–500 °C). The CO conversion ratios of Co–Fe<sub>2</sub>O<sub>3</sub>/

RHA, Cu–Fe<sub>2</sub>O<sub>3</sub>/RHA, and Fe<sub>2</sub>O<sub>3</sub>/RHA catalysts exhibit an upward trend with an increase in temperature. Notably, the Co–Fe<sub>2</sub>O<sub>3</sub>/RHA catalyst attains 100% CO conversion within the temperature range of 100–500 °C. Meanwhile, the Cu–Fe<sub>2</sub>O<sub>3</sub>/RHA catalyst achieves 100% CO conversion at 200–500 °C. The Fe<sub>2</sub>O<sub>3</sub>/RHA catalyst surpasses 80% CO conversion exclusively at temperatures exceeding 300 °C. Therefore, all doping of Cu, Co, or Ce can promote CO conversion, in which Ce doping emerges as the most effective in boosting CO conversion, followed closely by Co, with Cu trailing behind.

As depicted in Figure 1(b), all four catalysts demonstrate an ascending trend in the NO<sub>x</sub> conversion ratio with the increase in temperature. Both Co–Fe<sub>2</sub>O<sub>3</sub>/RHA and Cu–Fe<sub>2</sub>O<sub>3</sub>/RHA catalysts notably outperformed, achieving NO<sub>x</sub> conversion ratios of over 98.5% in the temperature range of 100–500 °C. The NO<sub>x</sub> conversion ratio of Co–Fe<sub>2</sub>O<sub>3</sub>/RHA (60.8%) is greater than that of Cu–Fe<sub>2</sub>O<sub>3</sub>/RHA (35.3%) at 25 °C. In addition, the NO<sub>x</sub> conversion ratio of Ce–Fe<sub>2</sub>O<sub>3</sub>/RHA is greater than 80% at 300–500 °C, reaching a maximum value of 94.5% at 500 °C. The lowest NO<sub>x</sub> conversion ratio, less than 80%, was achieved with the Fe<sub>2</sub>O<sub>3</sub>/RHA catalyst at temperatures below 400 °C. Consequently, Co doping is the most effective for NO<sub>x</sub> removal, and Cu doping excels at temperatures above 100 °C, whereas Ce doping demonstrates the least efficacy.

Upon analysis of N<sub>2</sub> selectivity as depicted in Figure 1(c), both Co–Fe<sub>2</sub>O<sub>3</sub>/RHA and Cu–Fe<sub>2</sub>O<sub>3</sub>/RHA catalysts stand out, consistently achieving nearly 100% across the temperature range of 25–500 °C. In comparison, the N<sub>2</sub> selectivity of the Ce–Fe<sub>2</sub>O<sub>3</sub>/RHA catalyst is inferior to that of the Fe<sub>2</sub>O<sub>3</sub>/RHA catalyst. Interestingly, as the temperature increases, the N<sub>2</sub> selectivity of the Ce–Fe<sub>2</sub>O<sub>3</sub>/RHA and Fe<sub>2</sub>O<sub>3</sub>/RHA catalysts initially dips and subsequently climbs, presenting an inverse trend to the N<sub>2</sub>O concentration curve (Figure 1d). This suggests an inclination toward N<sub>2</sub>O desorption at lower temperatures, shifting to decomposition into N<sub>2</sub> at higher temperatures, agreeing well with previous studies.<sup>28,35</sup> This is because N<sub>2</sub>O is not only a waste byproduct but also an important intermediate that can be further decomposed to produce N<sub>2</sub>. The desorption or decomposition of N<sub>2</sub>O molecules depends on whether the temperature can provide enough energy to cross the energy barrier for the decomposition of N<sub>2</sub>O into N<sub>2</sub>.<sup>36</sup> In addition, Table S1 shows the catalytic activity for the NO<sub>x</sub> reduction of selected representative SCR catalysts, and the comparative results demonstrate the high CO-SCR activity of the Co–Fe<sub>2</sub>O<sub>3</sub>/RHA catalyst at low temperatures.

In summary, the Co–Fe<sub>2</sub>O<sub>3</sub>/RHA catalyst emerges as the frontrunner, showcasing outstanding CO-SCR activity over a broad temperature window from 100 to 500 °C at an O<sub>2</sub> concentration of 6%, with its metrics for CO conversion ratio, NO<sub>x</sub> conversion ratio, and N<sub>2</sub> selectivity all exceeding 98.5%. The Cu–Fe<sub>2</sub>O<sub>3</sub>/RHA catalyst also performs well within the 150–500 °C range. Conversely, while the Ce–Fe<sub>2</sub>O<sub>3</sub>/RHA catalyst displays a commendable CO conversion ratio, it falls short in the domains of the NO<sub>x</sub> conversion ratio and N<sub>2</sub> selectivity.

**3.1.2. Catalytic Performance of Co–Fe<sub>2</sub>O<sub>3</sub>/RHA for CO-SCR.** The catalytic efficacy of the Co–Fe<sub>2</sub>O<sub>3</sub>/RHA catalyst for CO-SCR was evaluated across a range of O<sub>2</sub> concentrations (0–10%) and reaction temperatures (25–500 °C). The test stream consisted of 200 ppm NO, 2000 ppm CO, varying O<sub>2</sub>

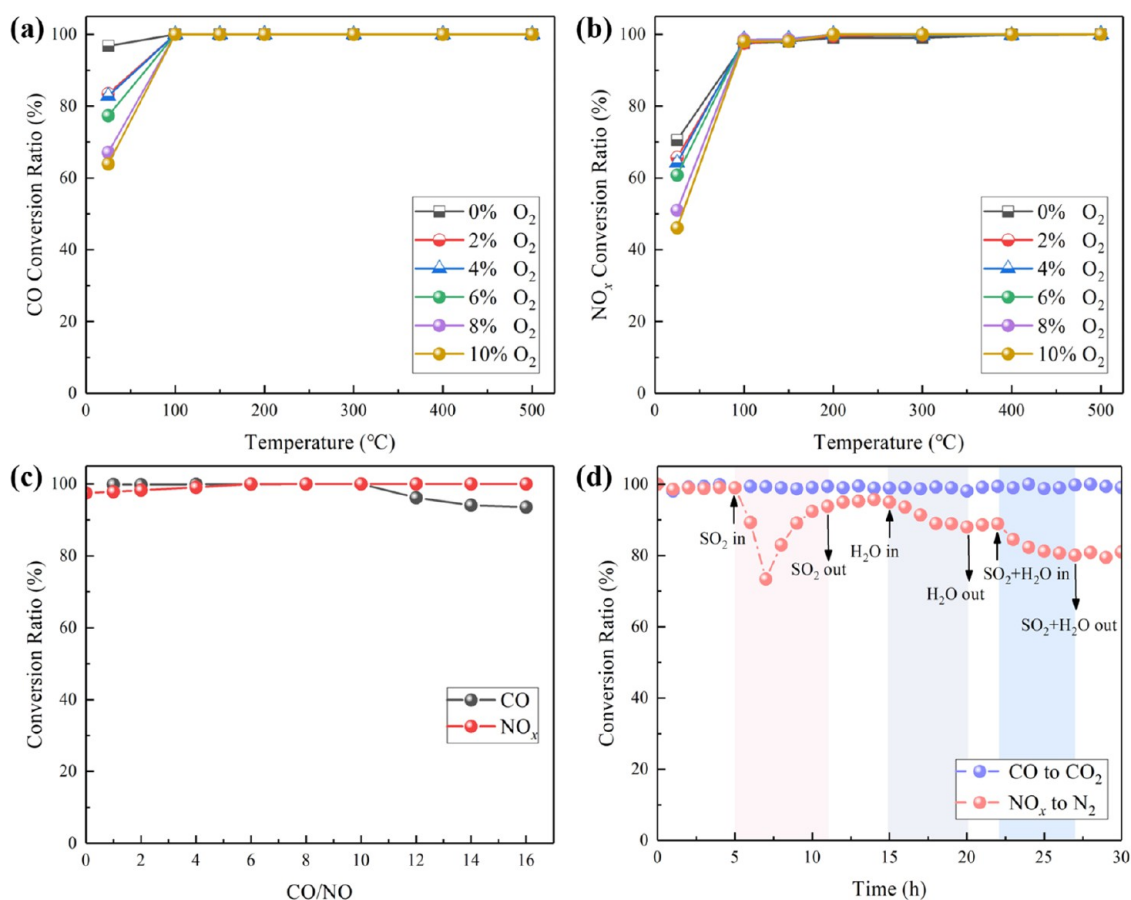


**Figure 2.** CO-SCR activity of the Co-Fe<sub>2</sub>O<sub>3</sub>/RHA catalyst. (a) CO conversion ratio and (b) NO<sub>x</sub> conversion ratio at different O<sub>2</sub> concentrations and temperatures. (c) CO-SCR performance at different CO/NO ratios. (d) H<sub>2</sub>O and SO<sub>2</sub> resistance.

concentrations, and N<sub>2</sub> making up the balance. As illustrated in Figure 2(a), higher O<sub>2</sub> concentrations slightly suppressed the CO conversion at 25 °C. However, this influence diminishes as the temperature increases. Remarkably, the CO conversion ratio remains steadfast, hovering around 100% from 100 to 500 °C, irrespective of the O<sub>2</sub> concentration and temperature variations. It is pivotal to mention that the 0% O<sub>2</sub> condition referenced here is not an absolute null value but approximates it, owing to the inevitable minor air influx via the induced draft system of the flue gas analyzer. This systemic error particularly impacts the 0% condition but becomes inconsequential when mimicking the presence of O<sub>2</sub> in exhaust gases. The NO<sub>x</sub> conversion ratios at different oxygen concentrations (Figure 2b) are all below 80% at 25 °C and above 97.5% at 100–500 °C, highlighting the good ability of the Co-Fe<sub>2</sub>O<sub>3</sub>/RHA catalyst to resist O<sub>2</sub> poisoning and its superior catalytic activity over a wide temperature range.

The effect of the CO/NO ratio on the Co-Fe<sub>2</sub>O<sub>3</sub>/RHA catalyst's performance was evaluated under simulated flue gas conditions containing 6% oxygen at 100 °C by adjusting the CO/NO ratios. Figure 2(c) demonstrates that the catalyst sustains high CO-SCR activity across various CO/NO ratios, consistently achieving near 100% conversion for both CO and NO<sub>x</sub> within the 6–10 ratio range. Notably, when the ratio dips below 6, there is a minor decline in NO<sub>x</sub> conversion. This may stem from an inadequate reductant supply, leading to a shortfall in surface oxygen vacancies essential for NO<sub>x</sub> decomposition.<sup>36</sup> Conversely, once the CO/NO ratio surpasses 10, the level of CO conversion starts to decline,

albeit remaining above 93%. This trend might be a consequence of the competitive adsorption between CO and NO<sub>x</sub>. A surplus of CO in the reaction mixture might induce partial catalyst surface blockage. Intriguingly, in the absence of CO within the simulated flue gas, the NO<sub>x</sub> conversion ratio of the Co-Fe<sub>2</sub>O<sub>3</sub>/RHA catalyst is close to 97.5%. This phenomenon can be ascribed to the catalyst's robust adsorption capability, possibly leading to the physical adsorption of NO<sub>x</sub>. Prior research has shown that Fe<sub>2</sub>O<sub>3</sub>-based catalysts can promote the direct decomposition of NO<sub>x</sub> without the use of reducing agents, but this process requires stringent conditions and does not ensure persistence and stability of performance.<sup>34</sup> Thus, the use of reducing agents remains a prudent strategy for evaluating the catalyst's efficacy. In short, the Co-Fe<sub>2</sub>O<sub>3</sub>/RHA catalyst shows superior performance in the coremoval of CO and NO<sub>x</sub>.

To ascertain the catalyst's viability for industrial applications, its resilience to hydrothermal conditions and resistance to potential contaminants, specifically SO<sub>2</sub> and H<sub>2</sub>O (g), was examined at 100 °C. The simulated flue gas consisted of 200 ppm NO, 2000 ppm CO, and 6% O<sub>2</sub>, balanced by N<sub>2</sub>, with varying concentrations of SO<sub>2</sub> (0 or 140 ppm) and H<sub>2</sub>O (g) (0 or 2 vol %). As shown in Figure 2(d), the CO conversion ratio is stable at over 98%, even in the face of SO<sub>2</sub> and H<sub>2</sub>O (g). The NO<sub>x</sub> conversion ratio is significantly impacted by the coaction of H<sub>2</sub>O (g) and SO<sub>2</sub> but shows a reversible decline and then a slow increase when SO<sub>2</sub> is introduced alone, i.e., it decreases from nearly 100 to 73.4% and gradually rises back to about 92.4%. Once SO<sub>2</sub> is withdrawn, the NO<sub>x</sub> conversion ratio

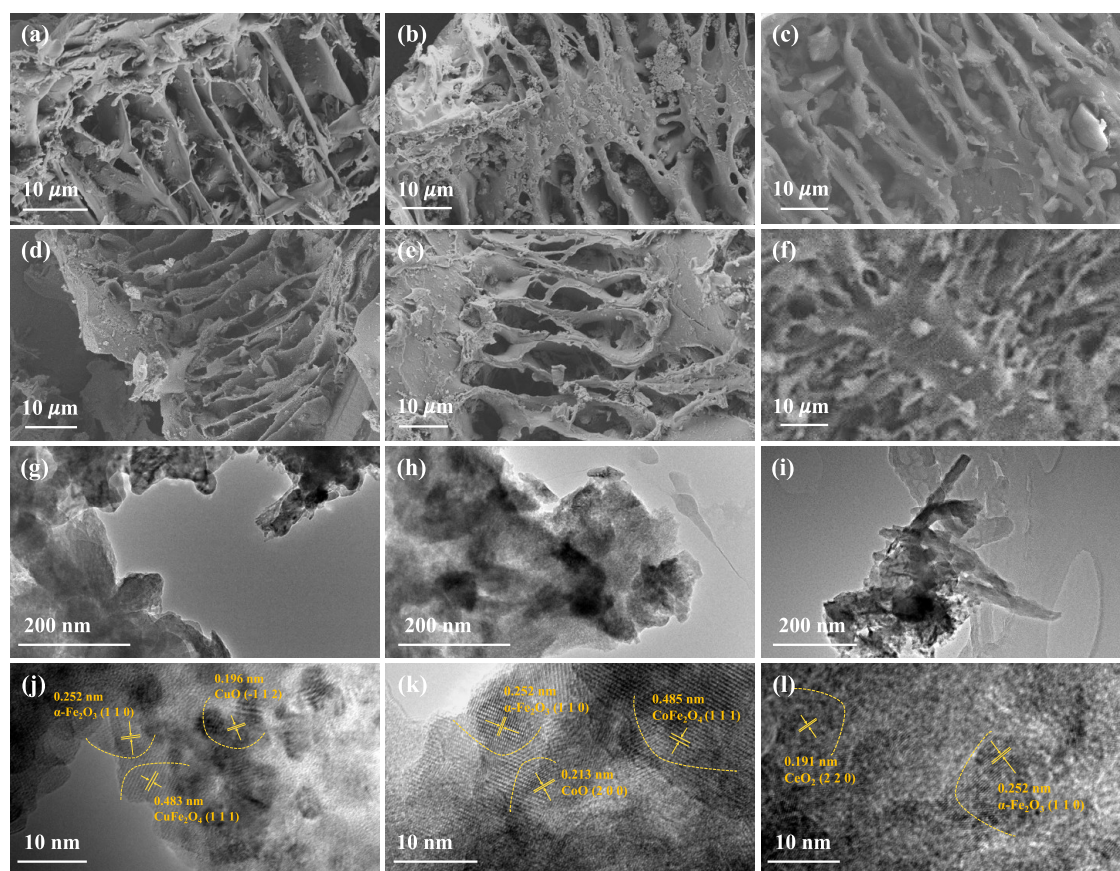


**Figure 3.** Structural and textural properties of metal-doped Fe<sub>2</sub>O<sub>3</sub>-based catalysts. (a–f) SEM images of the three catalysts before and after the activity experiment: (a) Cu–Fe<sub>2</sub>O<sub>3</sub>/RHA, (b) Co–Fe<sub>2</sub>O<sub>3</sub>/RHA, (c) Ce–Fe<sub>2</sub>O<sub>3</sub>/RHA, (d) Cu–Fe<sub>2</sub>O<sub>3</sub>/RHA-U, (e) Co–Fe<sub>2</sub>O<sub>3</sub>/RHA-U, and (f) Ce–Fe<sub>2</sub>O<sub>3</sub>/RHA-U. (g–i) TEM images of the three catalysts at 100 nm magnification: (g) Cu–Fe<sub>2</sub>O<sub>3</sub>/RHA, (h) Co–Fe<sub>2</sub>O<sub>3</sub>/RHA, and (i) Ce–Fe<sub>2</sub>O<sub>3</sub>/RHA. (j–l) TEM images of the three catalysts at 10 nm magnification: (j) Cu–Fe<sub>2</sub>O<sub>3</sub>/RHA, (k) Co–Fe<sub>2</sub>O<sub>3</sub>/RHA, and (l) Ce–Fe<sub>2</sub>O<sub>3</sub>/RHA.

returns to around 95.7%. The presence of H<sub>2</sub>O (g) results in a nonrecoverable drop in the NO<sub>x</sub> conversion ratio to about 88%. The combined introduction of H<sub>2</sub>O (g) and SO<sub>2</sub> amplifies this reduction, pushing the ratio to about 80.1%, a level that remains unchanged even after the withdrawn SO<sub>2</sub> and H<sub>2</sub>O. Notably, the Co–Fe<sub>2</sub>O<sub>3</sub>/RHA catalyst persistently achieves over 98% CO conversion and approximately 80.1% NO<sub>x</sub> conversion even after enduring a 30 h antipoisoning test. These results underscore the catalyst's good resistance to SO<sub>2</sub> and H<sub>2</sub>O (g), emphasizing its promising potential for broader industrial deployment.

**3.2. Characterizations Results.** **3.2.1. Structural and Textural Properties.** Figure 3(a–c) showcases SEM images of the fresh unused Cu–Fe<sub>2</sub>O<sub>3</sub>/RHA, Co–Fe<sub>2</sub>O<sub>3</sub>/RHA, and Ce–Fe<sub>2</sub>O<sub>3</sub>/RHA catalysts at 10 μm magnification, emphasizing their unique surface morphology. All catalyst samples display a rugged surface texture, an intrinsic RHA skeleton structure, evenly dispersed metal oxide particles, and a diversity of pore dimensions. Meanwhile, Figure 3(d–f) provides SEM images of the used catalysts (labeled with a “U” suffix after more than 16 h of activity testing). These images reveal negligible alterations in microstructure, pointing to superior structural stability. The metal oxide particles sustain their distinct form without evident sintering or aggregation, and the RHA maintains the skeleton structure rich in slit pores. Such findings underscore the remarkable stability of these RHA-supported metal oxide catalysts, corroborating the consistent

CO-SCR performance observed during the reaction assessment.

Figure 3(g–l) presents high-resolution transmission electron microscopy (HRTEM) images of Cu–Fe<sub>2</sub>O<sub>3</sub>/RHA, Co–Fe<sub>2</sub>O<sub>3</sub>/RHA, and Ce–Fe<sub>2</sub>O<sub>3</sub>/RHA catalysts at magnifications of 200 and 10 nm, underlining the uniform distribution of metal oxide crystallites on the RHA support. This underscores RHA's effectiveness as catalyst support that promotes uniform dispersion of metal particles. The TEM images of all three catalysts indicate an absence of significant particle clustering, aligning with the SEM findings. Notably, the lattice fringes observed in the TEM images at the 10 nm scale can be ascribed to various crystalline facets, such as α-Fe<sub>2</sub>O<sub>3</sub> (110), CuO (112), CuFe<sub>2</sub>O<sub>4</sub> (111), CoO (200), CoFe<sub>2</sub>O<sub>4</sub> (111), and CeO<sub>2</sub> (220). Among these, the α-Fe<sub>2</sub>O<sub>3</sub> (110) facet prevails, highlighting its significance as the principal crystalline phase with outstanding redox properties. The uniform distribution of metal oxides and their evident crystallinity, seen in HRTEM images, offers insights into the remarkable functionality of these catalysts. Moreover, Figures S3–S5 show the EDS images of Cu–Fe<sub>2</sub>O<sub>3</sub>/RHA, Co–Fe<sub>2</sub>O<sub>3</sub>/RHA, and Ce–Fe<sub>2</sub>O<sub>3</sub>/RHA catalysts, which further demonstrate the well-dispersed nature of the metal oxide active components on the RHA surface, in line with the SEM and TEM findings. The elemental analysis of prepared catalysts (Table S2) reveals that the ratio of iron to dopant metal was about 2:1 and the catalysts were successfully prepared as expected.

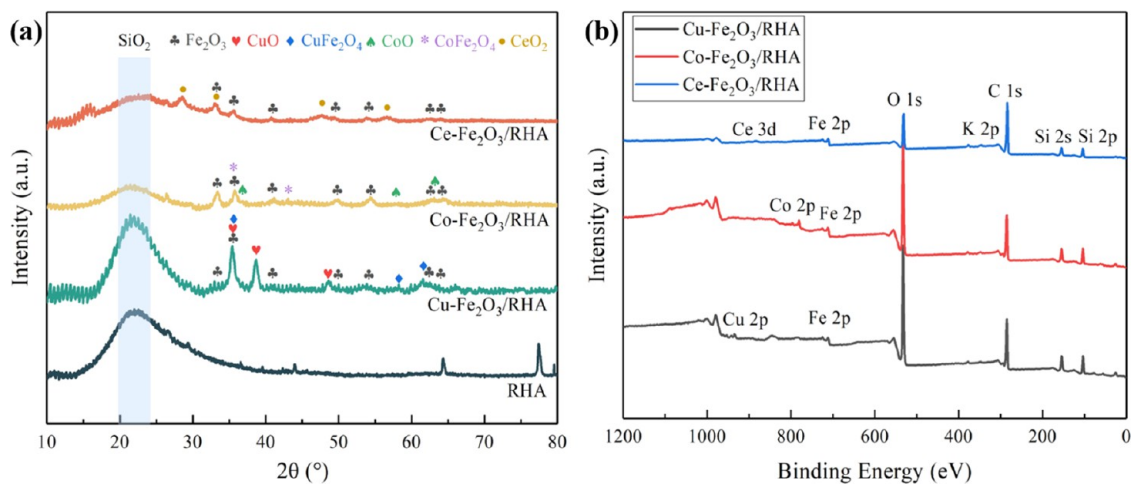


**Figure 4.** Phase composition and elemental valence states of metal-doped  $\text{Fe}_2\text{O}_3$ -based catalysts: (a) XRD patterns and (b) XPS full spectra.

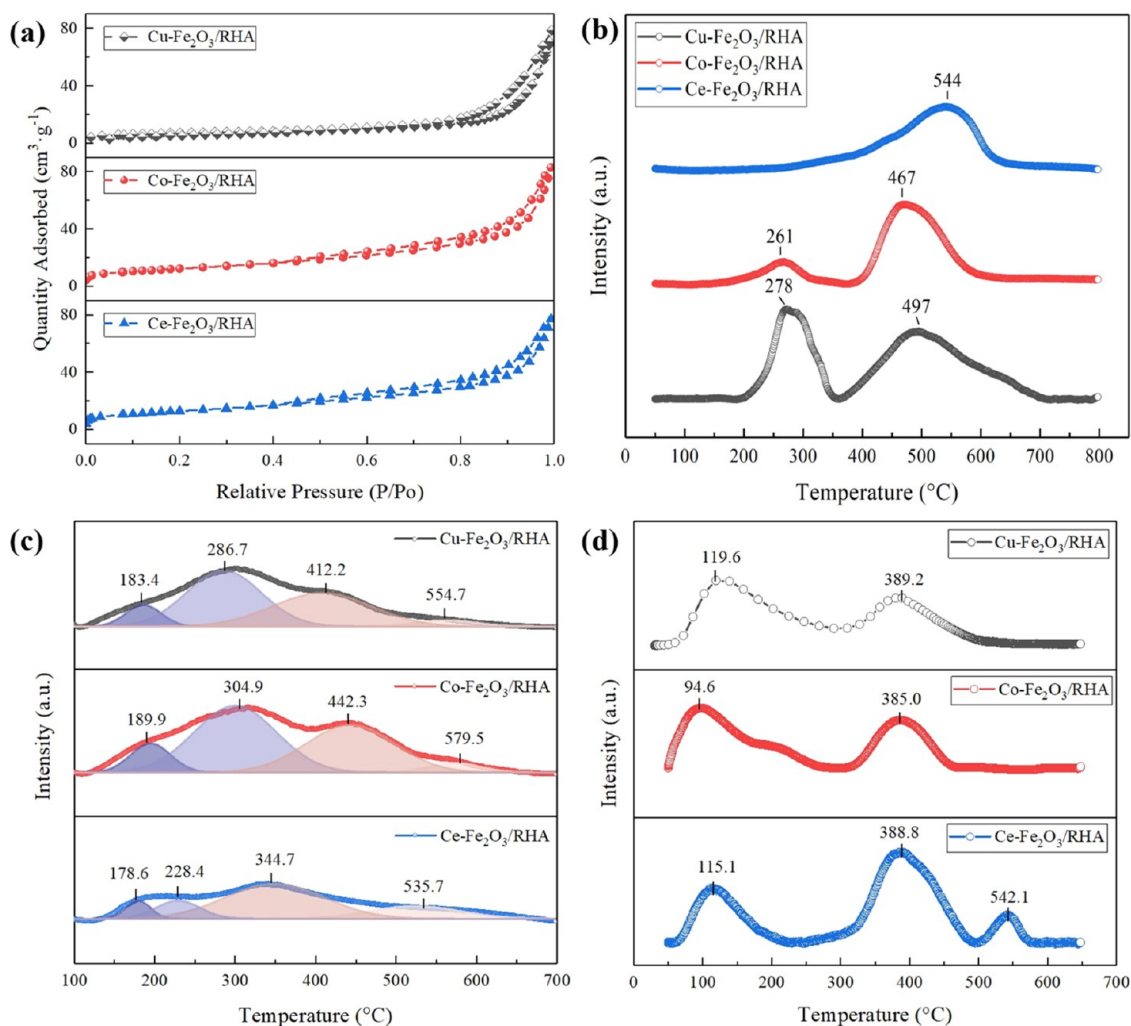


**Figure 5.** Physical adsorption properties, redox ability, and acidity of metal-doped  $\text{Fe}_2\text{O}_3$ -based catalysts: (a) BET, (b)  $\text{H}_2$ -TPR, (c)  $\text{NH}_3$ -TPD, and (d)  $\text{CO}_2$ -TPD.

### 3.2.2. Phase Composition and Elemental Valence States.

The XRD patterns depicted in Figure 4(a) confirm the successful synthesis of  $\text{Cu-Fe}_2\text{O}_3/\text{RHA}$ ,  $\text{Co-Fe}_2\text{O}_3/\text{RHA}$ , and  $\text{Ce-Fe}_2\text{O}_3/\text{RHA}$  catalysts. All of them exhibit broad “steamed bun” diffraction peaks along with characteristic

diffraction peaks of the standard hematite phase (PDF#87-1166), which, respectively, correspond to the amorphous  $\text{SiO}_2$  in RHA and crystalline  $\alpha\text{-Fe}_2\text{O}_3$ . Additionally, distinct diffraction peaks can be identified for  $\text{CuO}$  and  $\text{CuFe}_2\text{O}_4$  in  $\text{Cu-Fe}_2\text{O}_3/\text{RHA}$ , for  $\text{CoO}$  and  $\text{CoFe}_2\text{O}_4$  in  $\text{Co-Fe}_2\text{O}_3/\text{RHA}$ ,

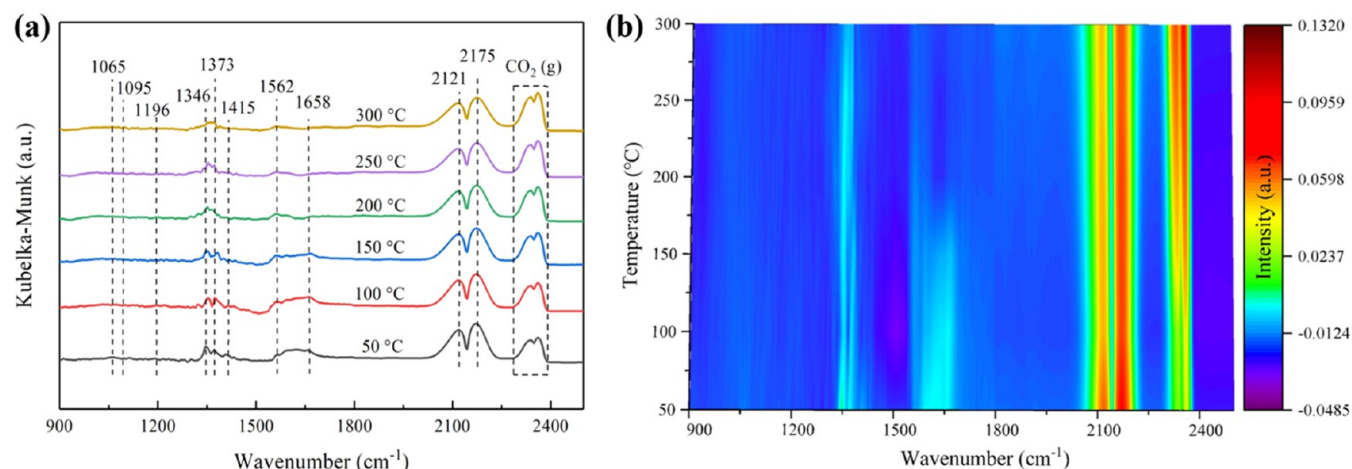


**Figure 6.** In situ DRIFTS spectra of NO + CO + O<sub>2</sub> coadsorption on the Co-Fe<sub>2</sub>O<sub>3</sub>/RHA surface at different temperatures: (a) line graph and (b) two-dimensional (2D) projection.

and for CeO<sub>2</sub> in Ce-Fe<sub>2</sub>O<sub>3</sub>/RHA. The findings observed by XRD are in agreement with the TEM results.

Determining the active species on the catalyst's surface is pivotal for redox reactions. As shown in Figure 4(b), the XPS spectra of the catalysts verify the presence of elements, such as Si, C, K, and O, Fe, Cu (in Cu-Fe<sub>2</sub>O<sub>3</sub>/RHA), Co (in Co-Fe<sub>2</sub>O<sub>3</sub>/RHA), and Ce (in Ce-Fe<sub>2</sub>O<sub>3</sub>/RHA). The elements of Si, C, and K are derived from the RHA support. The peaks at 723.9 and 710.8 eV align with the spin orbitals Fe 2p<sub>1/2</sub> and Fe 2p<sub>3/2</sub>, respectively, indicating that the existing form of Fe in the three catalysts is mainly Fe<sub>2</sub>O<sub>3</sub>. Moreover, the peak of the Cu 2p<sub>3/2</sub> spin orbital is located at 933.8 eV and the evident satellite peak around 943 eV confirms the existence of CuO in Cu-Fe<sub>2</sub>O<sub>3</sub>/RHA. When compared to the standard CuO spectrum (Cu 2p<sub>3/2</sub> peak at 933.1 eV), the XPS curve of Cu-Fe<sub>2</sub>O<sub>3</sub>/RHA shows a subtle upward shift in the binding energy to 933.8 eV. This transformation suggests the possible formation of stronger Fe-O<sub>x</sub>-Cu bonds, possibly related to the CuFe<sub>2</sub>O<sub>4</sub> complex. Similarly, the peak at 780.8 eV for the spin orbital of Co 2p<sub>3/2</sub> suggests that Co, in the form of CoO, dominates the Co-Fe<sub>2</sub>O<sub>3</sub>/RHA catalyst. Notably, the Co 2p<sub>3/2</sub> peak in Co-Fe<sub>2</sub>O<sub>3</sub>/RHA shifts from its standard position of 779.7–780.8 eV, pointing to the presence of enhanced Fe-O<sub>x</sub>-Co bonds, associated with the CoFe<sub>2</sub>O<sub>4</sub> species. For Ce-Fe<sub>2</sub>O<sub>3</sub>/RHA, the peaks at 900.6 and 882 eV correspond to the spin orbitals Ce 3d<sub>3/2</sub> and Ce 3d<sub>5/2</sub>, confirming Ce predominantly as CeO<sub>2</sub>, aligning with XRD findings. In essence, the XPS insights corroborate the presence of Fe<sub>2</sub>O<sub>3</sub>, CuO, CoO, and CeO<sub>2</sub>. Some Fe combined with Cu/Co forms CuFe<sub>2</sub>O<sub>4</sub> or CoFe<sub>2</sub>O<sub>4</sub> compounds, potentially improving the catalyst's efficiency.

**3.2.3. Physical Adsorption Properties, Redox Ability, and Acidity.** It can be seen from Figure 5(a) that the hysteresis loops exist in the adsorption and desorption curves for the three catalysts. These curves align with type IV isotherms, which are characteristic of mesoporous materials. All three catalysts supported on RHA exhibit H3-type hysteresis loops. Notably, the H3 hysteresis loop lacks a clear saturation point in its adsorption profile, suggesting a notably irregular pore structure. Such a phenomenon implies that the predominant pores in these catalysts resemble flat-shaped slit mesopores, resulting from the clustering of nonrigid agglomerates of plate-like particles.<sup>37</sup> This may represent the spaces formed by the inherent skeletal structure of RHA. In addition, Table S3

provides a comprehensive overview of the BET surface area, pore volume, and average pore size for each catalyst. Of these, Co-Fe<sub>2</sub>O<sub>3</sub>/RHA stands out with the highest specific surface area (46.448 m<sup>2</sup>·g<sup>-1</sup>), indicating a developed pore structure and robust adsorption capacity, which can enhance molecular adsorption and improve reaction efficiency. The BET metrics agree well with experimental findings, further emphasizing the excellent CO-SCR activity of Co-Fe<sub>2</sub>O<sub>3</sub>/RHA.

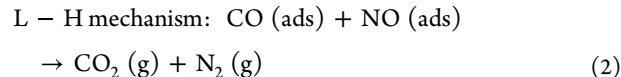
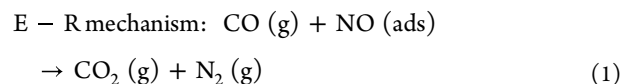
To gain insights into the improved low-temperature activity, we closely examined the redox capacity, acidity, and basicity of the Cu-Fe<sub>2</sub>O<sub>3</sub>/RHA, Co-Fe<sub>2</sub>O<sub>3</sub>/RHA, and Ce-Fe<sub>2</sub>O<sub>3</sub>/RHA catalysts. This investigation employed H<sub>2</sub>-TPR, NH<sub>3</sub>-TPD, and CO<sub>2</sub>-TPD, with the results illustrated in Figure 5(b–d), respectively. As shown in Figure 5(b), there are two distinct reduction peaks of Cu-Fe<sub>2</sub>O<sub>3</sub>/RHA, representing the reduction of different species. The emergence of a peak at 278 °C is assigned to the reduction of the Cu species finely distributed on the catalyst surface. In addition, the 497 °C peak likely stems from the reduction of Fe species within the Fe-O<sub>x</sub>-Cu structure.<sup>38</sup> The H<sub>2</sub>-TPR profile of Co-Fe<sub>2</sub>O<sub>3</sub>/RHA, however, is marked by a strong peak around 467 °C, related to the reduction of Fe-O<sub>x</sub>-Co. The weak peak at 261 °C can be attributed to the reduction of the highly dispersed Co species. Notably, the dominant peak near 467 °C masks other weak reduction peaks. This indicates the presence of stronger Fe-Co interactions, promoting the production of more Fe-O<sub>x</sub>-Co species and enhancing the activity. The Ce-Fe<sub>2</sub>O<sub>3</sub>/RHA catalyst exhibits only one reduction peak located at 544 °C, which is probably attributed to the reduction of Fe species.<sup>20</sup>

In comparison, Co-Fe<sub>2</sub>O<sub>3</sub>/RHA exhibits the lowest reduction peak temperature, suggesting that it is more likely to act as an electron acceptor and reduce to a lower oxidation state, followed by Cu-Fe<sub>2</sub>O<sub>3</sub>/RHA. This phenomenon could stem from the synergistic interactions between the doped oxides (Cu, Co) and Fe<sub>2</sub>O<sub>3</sub>, which enhance the reductive capability.<sup>39</sup> This verifies the excellent low-temperature CO-SCR activity of the Co-Fe<sub>2</sub>O<sub>3</sub>/RHA and Cu-Fe<sub>2</sub>O<sub>3</sub>/RHA catalysts. Importantly, Co-Fe<sub>2</sub>O<sub>3</sub>/RHA shows a strong interaction between Fe and the metal dopant, potentially accounting for its highest SCR activity. Conversely, Ce-Fe<sub>2</sub>O<sub>3</sub>/RHA, with its higher reduction peak temperature, indicates a weaker reductive performance, aligned with its lowest activity in the experiment.

As depicted in Figure 5(c), the NH<sub>3</sub>-TPD results reveal that all three catalysts present four NH<sub>3</sub> desorption peaks. Among them, Co-Fe<sub>2</sub>O<sub>3</sub>/RHA has the highest desorption temperatures, signifying the strongest acidity, succeeded closely by Cu-Fe<sub>2</sub>O<sub>3</sub>/RHA. On the other hand, Ce-Fe<sub>2</sub>O<sub>3</sub>/RHA demonstrates the lowest desorption temperatures, pointing to its weakest acidity. This sequence mirrors the SCR performance order observed in the activity experiments. Building on prior research, acidic sites in NH<sub>3</sub>-TPD curves are typically divided into weakly acidic (<200 °C), moderately acidic (200–400 °C), and strongly acidic (>400 °C).<sup>40</sup> Notably, Co-Fe<sub>2</sub>O<sub>3</sub>/RHA displays pronounced desorption peak areas at 304.9 and 442.3 °C, highlighting an abundance of medium-to-strong acid sites. The above results indicate that Co-Fe<sub>2</sub>O<sub>3</sub>/RHA has the strongest acidity and the largest number of medium-strong acidic sites, which are consistent with its superior catalytic activity. Additionally, the CO<sub>2</sub>-TPD data in Figure 5(d) reveals that Co-Fe<sub>2</sub>O<sub>3</sub>/RHA possesses the lowest alkalinity, as evidenced by its minimal CO<sub>2</sub> desorption peak temperature. This aligns with its strongest acidity, as seen from the NH<sub>3</sub>-TPD data. Such properties of strong acidity and weak alkalinity are not conducive to SO<sub>2</sub> adsorption and sulfate accumulation, which likely accounts for the remarkable resistance to SO<sub>2</sub> of the Co-Fe<sub>2</sub>O<sub>3</sub>/RHA catalyst, as depicted in Figure 2(d).

**3.2.4. In Situ DRIFTS of the Coadsorption of CO, NO, and O<sub>2</sub>.** In order to decode the underlying mechanism of the CO-SCR reaction catalyzed by Co-Fe<sub>2</sub>O<sub>3</sub>/RHA, in situ DRIFTS was utilized to monitor the coadsorption of NO, CO, and O<sub>2</sub> on the catalyst's surface. By examining temperatures between 50 and 300 °C, a relationship between spectra and temperature is discerned in Figure 6. Various nitrate species form on the Co-Fe<sub>2</sub>O<sub>3</sub>/RHA surface at 50 °C, comprising bridged bidentate nitrates (1065, 1196 cm<sup>-1</sup>), linear monodentate nitrites (1095 cm<sup>-1</sup>), chelating bidentate nitrates (1346, 1373 cm<sup>-1</sup>), and isolated NO<sub>3</sub><sup>-</sup> (1415 cm<sup>-1</sup>). Carbonate-related peaks are also evident, highlighting carboxylate-type species (1562 cm<sup>-1</sup>) and bidentate carbonates (1658 cm<sup>-1</sup>). Additionally, the P and R branches of gaseous CO (2121 and 2175 cm<sup>-1</sup>) and the bands corresponding to gaseous CO<sub>2</sub> (2300–2400 cm<sup>-1</sup>) are detectable.<sup>32,41,42</sup> Notably, as temperature increases from 50 to 300 °C, the intensity in the 2300–2400 cm<sup>-1</sup> region increases, whereas the peaks at 2121 and 2175 cm<sup>-1</sup> diminish. This means that an increase in temperature can promote the consumption of CO and the production of CO<sub>2</sub>.<sup>26</sup> Concurrently, the intensities of both nitrate and carbonate peaks markedly recede from 50 to 300 °C, aligning with experimental data and underscoring the enhanced CO-SCR efficacy of Co-Fe<sub>2</sub>O<sub>3</sub>/RHA as temperature ascends.

The current consensus is that the SCR reaction, when catalyzed by supported metal oxide catalysts, adheres to a combination of Langmuir–Hinshelwood (L–H) and Eley–Rideal (E–R) mechanisms.<sup>31,43</sup> Both the L–H and E–R mechanisms are represented in eqs 1 and 2. Since no peaks of gaseous NO were found, it indicates that NO species mainly exist on the catalyst surface in the adsorbed state. At temperatures below 150 °C, the peaks of gaseous CO and adsorbed nitrate species decreased significantly with increasing temperatures, indicating that the E–R mechanism is followed at lower temperatures. The peaks of carbonate species decreased significantly from 150 to 300 °C, suggesting that the L–H mechanism is dominant at higher temperatures.<sup>44</sup>



**3.3. Promotional Mechanism of Metal Doping on the CO-SCR Activity of Fe<sub>2</sub>O<sub>3</sub>-Based Catalysts.** Based on the in situ DRIFTS analysis, the CO-SCR reaction on the Co-Fe<sub>2</sub>O<sub>3</sub>/RHA catalyst is driven by the combination of L–H and E–R mechanisms. The catalytic mechanism for CO-SCR over the Co-Fe<sub>2</sub>O<sub>3</sub>/RHA surface is illustrated in Figure 7. The

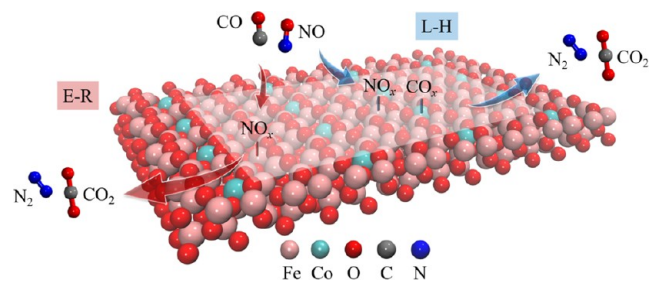


**Figure 7.** Catalytic mechanism of CO-SCR on the surface of Fe–Co bimetal catalysts.

detailed reaction mechanism is described as follows: At lower temperatures, gaseous CO molecules engage with free radicals ([N], [O]), which are generated from the decomposition of adsorbed nitrate species, resulting in the formation of CO<sub>2</sub> and N<sub>2</sub>. In contrast, at higher temperatures, the adsorbed carbonate species on the Fe–O<sub>x</sub>–Co active sites also react with the adsorbed nitrate species. These processes align with the E–R and L–H mechanisms, respectively. This research highlights the dopant metal's capacity to generate new active sites, thereby fostering the development of an enhanced composite catalyst with binuclear sites.<sup>45,46</sup>

Experimental analyses have concluded that the Co-Fe<sub>2</sub>O<sub>3</sub>/RHA catalyst exhibits outstanding CO-SCR activity, evidenced by its more than 98.5% CO and NO<sub>x</sub> conversion across a temperature range of 100–500 °C. Furthermore, it demonstrates good resistance to water and SO<sub>2</sub>. This excellent performance can be ascribed to several structure–performance relationships detailed below. First, a pivotal factor of the catalyst's remarkable CO-SCR activity lies in the double redox internal cycle shared between Fe<sub>2</sub>O<sub>3</sub> and CoO species (Fe<sup>3+</sup> ↔ Fe<sup>2+</sup>, Co<sup>2+</sup> ↔ Co<sup>3+</sup>). The strong synergy between RHA and Fe–Co species yields a greater number of Fe–O<sub>x</sub>–Co species and bimetallic active components, including CoFe<sub>2</sub>O<sub>4</sub> complexes. This facilitates improved redox characteristics and enhances the low-temperature SCR efficiency. Second, the stable structure of the RHA support guarantees high-temperature catalytic activity and hydrothermal stability. Third, the large specific surface area of the catalyst promotes strong adsorption capacity and efficient dispersion of active components, producing many evenly distributed active sites. Moreover, the catalyst exhibits enhanced acidity and abundant acidic sites, facilitating the promotion of SCR activity.<sup>47</sup> Due to its RHA support, which is rich in acidic oxide SiO<sub>2</sub>, the catalyst's alkalinity is consequently diminished, creating conditions that are unfavorable for the adsorption of SO<sub>2</sub> and the deposition of sulfates.<sup>34,36</sup> This characteristic may shed

light on the Co–Fe<sub>2</sub>O<sub>3</sub>/RHA catalyst's excellent resistance to SO<sub>2</sub>.

#### 4. CONCLUSIONS

In conclusion, a new Co–Fe<sub>2</sub>O<sub>3</sub>/RHA catalyst, characterized by its low cost and superior activity at low temperatures, was synthesized for CO-SCR through strategic metal doping. The proposed catalyst achieves conversion ratios for CO and NO<sub>x</sub> along with N<sub>2</sub> selectivity, exceeding 98.5% across a broad temperature window of 100–500 °C. Among various metals (Co, Cu, and Ce) considered for doping, Co emerged as the most effective. The enhanced efficacy of the Fe<sub>2</sub>O<sub>3</sub>-based catalyst by Co doping is ascribed to the strong Fe–O<sub>x</sub>–Co interaction alongside improved redox capability and acidic property. The CO-SCR reaction over the Co–Fe<sub>2</sub>O<sub>3</sub>/RHA catalyst adheres to the E–R mechanism at lower temperatures and transitions to the L–H mechanism at higher temperatures. The Co–Fe<sub>2</sub>O<sub>3</sub>/RHA catalyst exhibits outstanding behavior in the coremoval of CO and NO<sub>x</sub> with strong tolerance to O<sub>2</sub>, H<sub>2</sub>O (g), and SO<sub>2</sub>, underscoring its significant industrial applicability. This study unveils a cost-effective heterogeneous catalyst by metal doping and biomass reuse, offering guidance for the industrial adoption of CO-SCR technology with near-zero emission at low temperatures.

#### ■ ASSOCIATED CONTENT

##### SI Supporting Information

The Supporting Information is available free of charge at <https://pubs.acs.org/doi/10.1021/acsomega.4c00593>.

Experiment details (catalyst preparation, activity experiment, and characterizations); thermogravimetric analysis of uncalcined Cu–Fe<sub>2</sub>O<sub>3</sub>/RHA, Co–Fe<sub>2</sub>O<sub>3</sub>/RHA, and Ce–Fe<sub>2</sub>O<sub>3</sub>/RHA catalysts (TG, DTG, DSC); activity system of CO-SCR; EDS images of the Cu–Fe<sub>2</sub>O<sub>3</sub>/RHA catalyst, Co–Fe<sub>2</sub>O<sub>3</sub>/RHA catalyst, and Ce–Fe<sub>2</sub>O<sub>3</sub>/RHA catalyst; catalytic activity for NO<sub>x</sub> reduction of selected representative SCR catalysts; elemental analysis of prepared catalysts and BET data for the three catalysts (PDF)

#### ■ AUTHOR INFORMATION

##### Corresponding Authors

**Qulan Zhou** – State Key Laboratory of Multiphase Flow in Power Engineering, Xi'an Jiaotong University, Xi'an 710049, China; [orcid.org/0000-0002-6387-1052](https://orcid.org/0000-0002-6387-1052); Email: [qlzhou@mail.xjtu.edu.cn](mailto:qlzhou@mail.xjtu.edu.cn)

**Ke Li** – Institute of Materials Research and Engineering (IMRE), Agency for Science, Technology and Research (A\*STAR), Singapore 138634, Republic of Singapore; [orcid.org/0000-0002-3140-3983](https://orcid.org/0000-0002-3140-3983); Email: [li\\_ke@imre.a-star.edu.sg](mailto:li_ke@imre.a-star.edu.sg)

##### Authors

**Yuqing Pan** – State Key Laboratory of Multiphase Flow in Power Engineering, Xi'an Jiaotong University, Xi'an 710049, China; [orcid.org/0000-0001-5626-5495](https://orcid.org/0000-0001-5626-5495)

**Na Li** – State Key Laboratory of Multiphase Flow in Power Engineering, Xi'an Jiaotong University, Xi'an 710049, China; [orcid.org/0000-0002-7975-4862](https://orcid.org/0000-0002-7975-4862)

**Chenyang Wu** – State Key Laboratory of Multiphase Flow in Power Engineering, Xi'an Jiaotong University, Xi'an 710049, China

Complete contact information is available at: <https://pubs.acs.org/10.1021/acsomega.4c00593>

#### Author Contributions

Y.P.: Conceptualization, methodology, writing—original draft preparation, writing—reviewing and editing. N.L.: Resources, software, formal analysis. C.W.: Investigation and data curation. Q.Z.: Supervision, project administration, funding acquisition. K.L.: Supervision, validation, visualization, writing—reviewing and editing.

#### Notes

The authors declare no competing financial interest.

#### ■ ACKNOWLEDGMENTS

This work is supported by the National Key Research and Development Program of China (2021YFC3001803), Instrumental Analysis Center of Xi'an Jiaotong University, and the program of China Scholarships Council.

#### ■ REFERENCES

- (1) Guo, K.; Ji, J.; Song, W.; Sun, J.; Tang, C.; Dong, L. Conquering ammonium bisulfate poison over low-temperature NH<sub>3</sub>-SCR catalysts: A critical review. *Appl. Catal., B* **2021**, *297*, No. 120388.
- (2) Wang, J.; Gao, F.; Dang, P.; Tang, X.; Lu, M.; Du, Y.; Zhou, Y.; Yi, H.; Duan, E. Recent advances in NO reduction with CO over copper-based catalysts: reaction mechanisms, optimization strategies, and anti-inactivation measures. *Chem. Eng. J.* **2022**, *450*, No. 137374.
- (3) Rudolph, J.; Jacob, C. R. Computational insights into the mechanism of the selective catalytic reduction of NO<sub>x</sub>: Fe-versus Cu-exchanged zeolite catalysts. *ACS Omega* **2019**, *4* (5), 7987–7993.
- (4) Heo, I.; You, Y. W.; Lee, J. H.; Schmieg, S. J.; Yoon, D. Y.; Kim, C. H. Urealess NO<sub>x</sub> reduction by carbon monoxide in simulated lean-burn exhausts. *Environ. Sci. Technol.* **2020**, *54* (13), 8344–8351.
- (5) Guo, K.; Ji, J.; Osuga, R.; Zhu, Y.; Sun, J.; Tang, C.; Kondo, J. N.; Dong, L. Construction of Fe<sub>2</sub>O<sub>3</sub> loaded and mesopore confined thin-layer titania catalyst for efficient NH<sub>3</sub>-SCR of NO<sub>x</sub> with enhanced H<sub>2</sub>O/SO<sub>2</sub> tolerance. *Appl. Catal., B* **2021**, *287*, No. 119982.
- (6) Lian, Z.; Wei, J.; Shan, W.; Yu, Y.; Radjenovic, P. M.; Zhang, H.; He, G.; Liu, F.; Li, J. F.; Tian, Z. Q.; He, H. Adsorption-induced active vanadium species facilitate excellent performance in low-temperature catalytic NO<sub>x</sub> abatement. *J. Am. Chem. Soc.* **2021**, *143* (27), 10454–10461.
- (7) Vuong, T. H.; Radnik, J.; Rabeah, J.; Bentrup, U.; Schneider, M.; Atia, H.; Armbruster, U.; Grünert, W.; Brückner, A. Efficient VO<sub>x</sub>/Ce<sub>1-x</sub>Ti<sub>x</sub>O<sub>2</sub> catalysts for low-temperature NH<sub>3</sub>-SCR: Reaction mechanism and active sites assessed by in situ/operando spectroscopy. *ACS Catal.* **2017**, *7* (3), 1693–1705.
- (8) Du, H.; Yang, S.; Li, K.; Shen, Q.; Li, M.; Wang, X.; Fan, C. Study on the performance of the Zr-modified Cu-SSZ-13 catalyst for low-temperature NH<sub>3</sub>-SCR. *ACS Omega* **2022**, *7* (49), 45144–45152.
- (9) Pan, K.; Yu, F.; Liu, Z.; Zhou, X.; Sun, R.; Li, W.; Zhao, H.; Liu, M.; Guo, X.; Dai, B. Enhanced low-temperature CO-SCR denitration performance and mechanism of two-dimensional CuCoAl layered double oxide. *J. Environ. Chem. Eng.* **2022**, *10* (3), No. 108030.
- (10) Zhang, Y.; Zhao, L.; Kang, M.; Chen, Z.; Gao, S.; Hao, H. Insights into high CO-SCR performance of CuCoAlO catalysts derived from LDH/MOFs composites and study of H<sub>2</sub>O/SO<sub>2</sub> and alkali metal resistance. *Chem. Eng. J.* **2021**, *426*, No. 131873.
- (11) Zhang, C.; Sun, C.; Wu, M.; Lu, K. Optimisation design of SCR mixer for improving deposit performance at low temperatures. *Fuel* **2019**, *237*, 465–474.
- (12) Sierra-Pereira, C. A.; Urquieta-González, E. A. Reduction of NO with CO on CuO or Fe<sub>2</sub>O<sub>3</sub> catalysts supported on TiO<sub>2</sub> in the presence of O<sub>2</sub>, SO<sub>2</sub> and water steam. *Fuel* **2014**, *118*, 137–147.
- (13) Huang, L.; Shi, Y.; Xiong, W.; Ding, Y.; Zhang, Y. Facile design of highly effective Fe-modified bimetallic Fe<sub>x</sub>Ni<sub>1-x</sub>-MOFs catalysts

with rodlike structures for low-temperature NO reduction by CO. *J. Mater. Sci.* **2021**, *56* (16), 9914–9928.

(14) Oton, L. F.; Oliveira, A. C.; de Araujo, J. C. S.; Araujo, R. S.; de Sousa, F. F.; Saraiva, G. D.; Lang, R.; Otubo, L.; Carlos da Silva Duarte, G.; Campos, A. Selective catalytic reduction of NO<sub>x</sub> by CO (CO-SCR) over metal-supported nanoparticles dispersed on porous alumina. *Adv. Powder Technol.* **2020**, *31* (1), 464–476.

(15) Zhang, Y.; Li, D.; Xin, G.; Ren, S. CO-Selective Catalytic Reduction of NO<sub>x</sub> in fluid catalytic cracking units and applications of the generated exhaust gas for enhanced shale gas recovery and sequestration. *Energy Fuels* **2023**, *37* (16), 11754–11764.

(16) Ren, D.; Gui, K.; Gu, S. Comparison of sulfur poisoning resistance of Ce/Mn doped  $\gamma$ -Fe<sub>2</sub>O<sub>3</sub> (0 0 1) surface in NH<sub>3</sub>-SCR reaction with DFT method. *Appl. Surf. Sci.* **2021**, *561*, No. 149847, DOI: 10.1016/j.apsusc.2021.149847.

(17) Paolucci, C.; Khurana, I.; Parekh, A. A.; Li, S.; Shih, A. J.; Li, H.; Di Iorio, J. R.; Albarracin-Caballero, J. D.; Yezerets, A.; Miller, J. T.; Delgass, W. N.; Ribeiro, F. H.; Schneider, W. F.; Gounder, R. Dynamic multinuclear sites formed by mobilized copper ions in NO<sub>x</sub> selective catalytic reduction. *Science* **2017**, *357* (6354), 898–903.

(18) Lyu, Z.; Niu, S.; Lu, C.; Zhao, G.; Gong, Z.; Zhu, Y. A density functional theory study on the selective catalytic reduction of NO by NH<sub>3</sub> reactivity of  $\alpha$ -Fe<sub>2</sub>O<sub>3</sub> (0 0 1) catalyst doped by Mn, Ti, Cr and Ni. *Fuel* **2020**, *267*, No. 117147.

(19) Sun, C.; Chen, W.; Jia, X.; Liu, A.; Gao, F.; Feng, S.; Dong, L. Comprehensive understanding of the superior performance of Sm-modified Fe<sub>2</sub>O<sub>3</sub> catalysts with regard to NO conversion and H<sub>2</sub>O/SO<sub>2</sub> resistance in the NH<sub>3</sub>-SCR reaction. *Chin. J. Catal.* **2021**, *42* (3), 417–430.

(20) Gao, Y.; Teng, S.; Wang, Z.; Wang, B.; Liu, W.; Liu, W.; Wang, L. Enhanced catalytic performance of cobalt and iron co-doped ceria catalysts for soot combustion. *J. Mater. Sci.* **2020**, *55* (1), 283–297.

(21) Dasireddy, V. D. B. C.; Likozar, B. Selective catalytic reduction of NO<sub>x</sub> by CO over bimetallic transition metals supported by multi-walled carbon nanotubes (MWCNT). *Chem. Eng. J.* **2017**, *326*, 886–900.

(22) Chen, Y.; Li, C.; Chen, J.; Tang, X. Self-prevention of well-defined-facet Fe<sub>2</sub>O<sub>3</sub>/MoO<sub>3</sub> against deposition of ammonium bisulfate in low-temperature NH<sub>3</sub>-SCR. *Environ. Sci. Technol.* **2018**, *52* (20), 11796–11802.

(23) Yan, X.; Liu, J.; Yang, Y.; Wang, Z.; Zheng, Y. A catalytic reaction scheme for NO reduction by CO over Mn-terminated LaMnO<sub>3</sub> perovskite: A DFT study. *Fuel Process. Technol.* **2021**, *216*, No. 106798.

(24) Cheng, X.; Wang, L.; Wang, Z.; Zhang, M.; Ma, C. Catalytic Performance of NO reduction by CO over activated semicoke supported Fe/Co catalysts. *Ind. Eng. Chem. Res.* **2016**, *55* (50), 12710–12722.

(25) Han, S.; Xuan, C.; Wang, L.; Zhang, X.; Shao, R.; Cheng, X.; Wang, Z. Synergistic reduction mechanism of NO<sub>x</sub> by NH<sub>3</sub> and CO catalyzed by Mn-Co oxides and the oxidation process of CO: In situ DRIFTS and DFT study. *Energy Fuels* **2023**, *37* (21), 16701–16715.

(26) Liu, H.; Liu, L.; Wei, L.; Chu, B.; Qin, Z.; Jin, G.; Tong, Z.; Dong, L.; Li, B. Preparation of three-dimensionally ordered macroporous MFe<sub>2</sub>O<sub>4</sub> (M = Co, Ni, Cu) spinel catalyst and its simultaneous catalytic application in CO oxidation and NO + CO reaction. *Fuel* **2020**, *272*, No. 117738.

(27) Zhou, Z.; Harold, M. P.; Luss, D. NO<sub>x</sub> reduction on ceria: Impact of lean-rich cycling. *Appl. Catal., B* **2019**, *240*, 79–91.

(28) Sun, R.; Yu, F.; Wan, Y.; Pan, K.; Li, W.; Zhao, H.; Dan, J.; Dai, B. Reducing N<sub>2</sub>O formation over CO-SCR systems with CuCe mixed metal oxides. *ChemCatChem* **2021**, *13* (11), 2709–2718.

(29) Liu, H.; Wu, Y.; Liu, L.; Chu, B.; Qin, Z.; Jin, G.; Tong, Z.; Dong, L.; Li, B. Three-dimensionally ordered macroporous Fe-doped ceria catalyst with enhanced activity at a wide operating temperature window for selective catalytic reduction of NO<sub>x</sub>. *Appl. Surf. Sci.* **2019**, *498*, No. 143780, DOI: 10.1016/j.apsusc.2019.143780.

(30) Liu, Z.; Yu, F.; Dong, D.; Gui, R.; Li, W.; Sun, R.; Wan, Y.; Dan, J.; Wang, Q.; Dai, B. Transition-metal-doped ceria carried on

two-dimensional vermiculite for selective catalytic reduction of NO with CO: Experiments and density functional theory. *Appl. Surf. Sci.* **2021**, *566*, No. 150704.

(31) Ou, X.; Chen, K.; Wei, L.; Deng, Y.; Li, J.; Li, B.; Dong, L. Effect of Co doping on magnetic and CO-SCR properties of  $\gamma$ -Fe<sub>2</sub>O<sub>3</sub>. *Ind. Eng. Chem. Res.* **2021**, *60* (16), 5744–5757.

(32) Zhang, Y.; Zhao, L.; Duan, J.; Bi, S. Insights into deNO<sub>x</sub> processing over Ce-modified Cu-BTC catalysts for the CO-SCR reaction at low temperature by in situ DRIFTS. *Sep. Purif. Technol.* **2020**, *234*, No. 116081.

(33) Gholami, Z.; Luo, G.; Gholami, F.; Yang, F. Recent advances in selective catalytic reduction of NO<sub>x</sub> by carbon monoxide for flue gas cleaning process: a review. *Catal. Rev.* **2021**, *63* (1), 68–119.

(34) Pan, Y.; Li, N.; Ran, S.; Wen, D.; Luo, Q.; Li, K.; Zhou, Q. Efficient catalysis for low-temperature CO Selective Catalytic Reduction over an Fe-Cu bimetal oxide catalyst supported on amorphous SiO<sub>2</sub>. *Ind. Eng. Chem. Res.* **2022**, *61* (28), 9991–10003.

(35) Liu, Z.; Yu, F.; Pan, K.; Zhou, X.; Sun, R.; Tian, J.; Wan, Y.; Dan, J.; Dai, B. Two-dimensional vermiculite carried CuCoCe catalysts for CO-SCR in the presence of O<sub>2</sub> and H<sub>2</sub>O: Experimental and DFT calculation. *Chem. Eng. J.* **2021**, *422*, No. 130099.

(36) Pan, Y.; Li, N.; Li, K.; Ran, S.; Wu, C.; Zhou, Q.; Liu, J.; Li, S. Enhanced low-temperature behavior of selective catalytic reduction of NO<sub>x</sub> by CO on Fe-based catalyst with looping oxygen vacancy. *Chem. Eng. J.* **2023**, *461*, No. 141814.

(37) Thommes, M.; Kaneko, K.; Neimark, A. V.; Olivier, J. P.; Rodriguez-Reinoso, F.; Rouquerol, J.; Sing, K. S. W. Physisorption of gases, with special reference to the evaluation of surface area and pore size distribution (IUPAC Technical Report). *Pure Appl. Chem.* **2015**, *87* (9–10), 1051–1069.

(38) Xiao, Z.; Jin, S.; Wang, X.; Li, W.; Wang, J.; Liang, C. Preparation, structure and catalytic properties of magnetically separable Cu-Fe catalysts for glycerol hydrogenolysis. *J. Mater. Chem.* **2012**, *22* (32), 16598–16605.

(39) Shen, Z.; Xing, X.; Wang, S.; Zheng, Z.; Lv, M. Low temperature CO oxidation from sintering flue gas on CuO-CeO<sub>2</sub>/AC-Fe catalyst. *Catal. Today* **2023**, *423*, No. 113988.

(40) Weng, X.; Meng, Q.; Liu, J.; Jiang, W.; Pattison, S.; Wu, Z. Catalytic oxidation of chlorinated organics over lanthanide perovskites: Effects of phosphoric acid etching and water vapor on chlorine desorption behavior. *Environ. Sci. Technol.* **2019**, *53* (2), 884–893.

(41) Wang, L.; Wang, Z.; Cheng, X.; Zhang, M.; Qin, Y.; Ma, C. In situ DRIFTS study of the NO + CO reaction on Fe-Co binary metal oxides over activated semi-coke supports. *RSC Adv.* **2017**, *7* (13), 7695–7710.

(42) Zhang, Q.; Wang, H.; Ning, P.; Song, Z.; Liu, X.; Duan, Y. In situ DRIFTS studies on CuO-Fe<sub>2</sub>O<sub>3</sub> catalysts for low temperature selective catalytic oxidation of ammonia to nitrogen. *Appl. Surf. Sci.* **2017**, *419*, 733–743.

(43) Srinivasan, A.; Depcik, C. Review of chemical reactions in the NO reduction by CO on rhodium/alumina catalysts. *Catal. Rev.* **2010**, *52* (4), 462–493.

(44) Li, X.; Ren, S.; Jiang, Y.; Chen, Z.; Wang, L.; Liu, M.; Chen, T. In situ IR spectroscopy study of NO removal over CuCe catalyst for CO-SCR reaction at different temperature. *Catal. Today* **2023**, *418*, No. 114082.

(45) Shan, Y.; He, G.; Du, J.; Sun, Y.; Liu, Z.; Fu, Y.; Liu, F.; Shi, X.; Yu, Y.; He, H. Strikingly distinctive NH<sub>3</sub>-SCR behavior over Cu-SSZ-13 in the presence of NO<sub>2</sub>. *Nat. Commun.* **2022**, *13* (1), No. 4606.

(46) Qu, W.; Liu, X.; Chen, J.; Dong, Y.; Tang, X.; Chen, Y. Single-atom catalysts reveal the dinuclear characteristic of active sites in NO selective reduction with NH<sub>3</sub>. *Nat. Commun.* **2020**, *11* (1), No. 1532.

(47) Li, X.; Ren, S.; Chen, Z.; Chen, L.; Wang, M.; Wang, L.; Wang, A. Promoting mechanism of CuO on catalytic performance of CeFe catalyst for simultaneous removal of NO<sub>x</sub> and CO. *Fuel* **2023**, *347*, No. 128435.